Slippery Liquid Infused Porous Surfaces (SLIPS) Condensation

By: Xiaoyu Chen

2022 Wang Chu Chien-Wen Award Recipient

Advisor: Dr. Solomon Adera

Mechanical Engineering, University of Michigan

Abstract

Water condensation is widely used to transfer heat or separating fluids in many industrial processes. For example, nearly 85% of the global electricity is generated through the steam (Rankine) cycle. Typically, due to the high surface energy of metals and their oxides, vapor condenses by forming a continuous liquid film in filmwise mode. Compared with the filmwise condensation (FWC) on high surface energy wetting (hydrophilic) surfaces, dropwise condensation (DWC) on non-wetting (hydrophobic) surface has higher heat transfer coefficient. DWC on textured hydrophobic has been demonstrated to improve the heat transfer rate by as much as an order of magnitude compared to FWC. Based on the current understanding[1,2], slippery liquid infused porous surfaces (SLIPS) are expected to exhibit even higher heat transfer coefficient than DWC due to improved droplet mobility which is manifested by smaller droplet departure radius and higher departure frequency. In this work, we measure the heat transfer coefficient on smooth hydrophilic, textured hydrophobic or superhydrophobic (SHB) and SLIPS copper tubes. Our experiments show higher heat transfer coefficient for DWC than FWC, nearly a three-fold increase in heat transfer rate. The measured small contact angle hysteresis for SLIPS suggests higher droplet mobility, which is a promise for higher heat transfer coefficient during phase change condensation.

Introduction

Condensation is a phase change phenomenon accompanied by large amount heat transferred. This is an essential part of many industrial processes, such as power supply industries[3,4] and thermal desalination[5,6]. However, dur to the high surface energy of metals, most of the condensation mode used in those industries are filmwise condensation (FWC)[7], during which the condensate forms an interconnected continuous liquid film on the cold surface, serving as a thermal resistance and lowering the heat transfer coefficient. On the contrary, condensate on hydrophobic surface[8] will form droplets (instead of a continuous liquid film), exposing the cold surface directly to the hot vapor, which facilitates the heat transfer rate during phase change. Due to this effect, dropwise condensation (DWC) usually has higher heat transfer coefficient compared than FWC[9-11]. On hydrophobic surfaces, condensate droplets experience four stages: nucleation (droplet formation from the vapor phase)[12], droplet growth[13], droplet coalescence[12], and departure (rolling off from the surface)[14]. During these processes, droplet mobility and early departure (smaller departure radius at higher frequency) are crucial for coalescence and rolling off, respectively. A smaller droplet departure radius would make droplets start to roll off at a smaller size and thus improve the rate of droplet sweeping and cleaning the surface, which will expose the cold surface again[15].

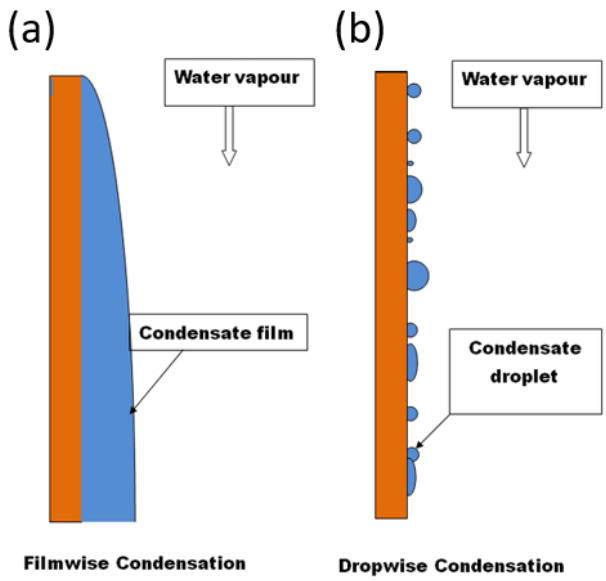

Figure 1. Dropwise condensation and filmwise condensation[16]. (a) Filmwise condensation will form a thin film of condensate, which acts as a thermal resistance for further heat transfer. (b) On the contrary, dropwise condensation will form discrete condensate droplets that shed off when gravity overcomes surface tension. The periodic removal of condensate droplets from the condensate surface improves the heat transfer rate by nearly an order of magnitude.

Recently discovered slippery liquid infused porous surfaces (SLIPS)[17] are also other approach to achieving dropwise condensation[18]. Droplets on SLIPS have extremely high mobility and smaller droplet departure radius compared to conventional non-wetting or superhydrophobic (SHB) surfaces. Therefore, in theory, condensation on SLIPS could reach a higher heat transfer coefficient.

The purpose of this research is to compare the heat transfer rate during steam condensation on hydrophilic (filmwise condensation, FWC), hydrophobic (dropwise condensation, DWC) and SLIPS condensation.

Filmwise Condensation

The heat transfer coefficient of FWC on the surface of a horizontal cylinder of diameter D is predicted by Nusselt model[7]. The thin liquid film covering the surface is assumed to be laminar flow.

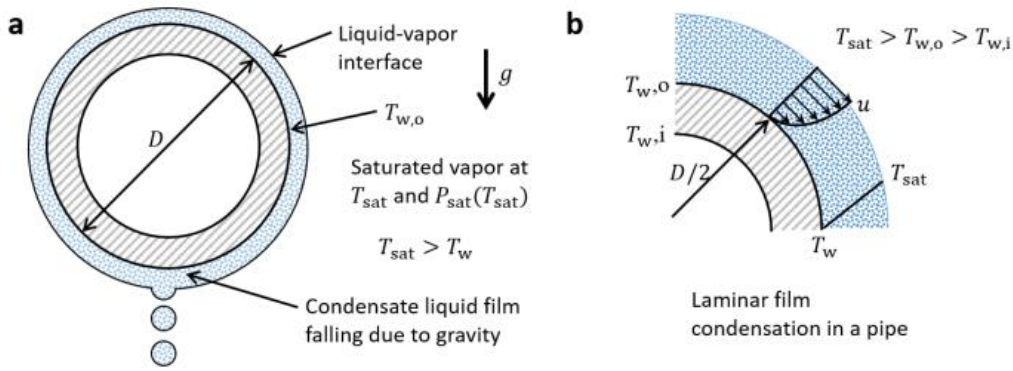

Figure 2. Nusselt model (film condensation on tubes)[19]. (a) The condensate liquid film thickness increases from the top to the bottom of the cylinder surface as the vapor continues to condense on the liquid-vapor interface. (b) The velocity and temperature profile of the condensate film.

The heat transfer coefficient is predicted as:

$$h_{c,fwc} = 0.729\left(\frac{g\rho_l(\rho_l - \rho_v)k_l^3 h'_{fg}}{\mu_l D\left(T_{sat} - T_{w,o}\right)}\right)^{\frac{1}{4}} \tag{1}$$

where g is gravity, ρ_l and ρ_v are liquid and vapor densities, μ_l is the dynamic viscosity of the condensate liquid and h'_{fg} is the modified latent heat of vapor-liquid phase change. We use Rohsenow correlation to account for the cooling of the condensate liquid from T_{sat} to $T_{w.o}$, which is given by:

$$h'_{fg} = h_{fg}(1 + 0.68Ja) \tag{2}$$

where the Jakob number (Ja) is:

$$Ja = \frac{c_{p,l}(T_{sat} - T_{w.o})}{h_{fg}} \tag{3}$$

Experiment

Sample Preparation

The hydrophilic tube used for FWC in the experiment is a smooth copper tube with untreated surface while the following chemical treatment was applied to the same tube to make it superhydrophobic for DWC.

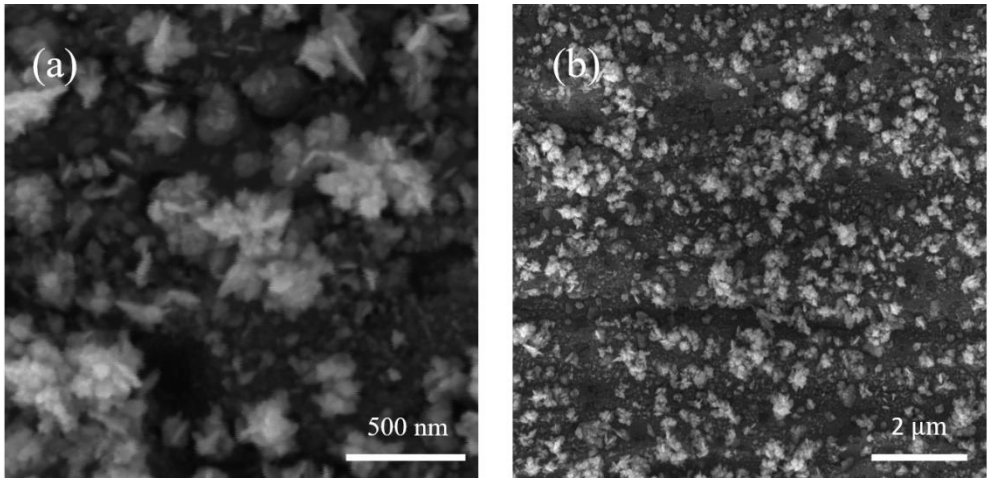

Figure 3. Scanning electron micrograph (SEM) images of the nanostructure copper surface at different magnifications before oil infusion.

First, the copper tube was sanded (to remove the oxide on top of the surface) and then immediately sonicated in acetone for five minutes. Then, it was immersed in 0.01 mol/L silver nitrate solution until the surface becomes black. Through chemical reaction, the silver has formed nanostructure on the copper surface as shown in Fig 3. After the black tube was cleaned by deionized water (DIW), it was put into 0.001mol/L heptadecafluoro-1-decanethiol dichloromethane solution for 5 minutes. Finally, it was rinsed with dichloromethane and then DIW. As for the SLIP surfaces, we infuse the tube with the lubricant oil (Krytox 100). And a thin film of oil will form after vertically placing the tube for ~15 minutes.

Experimental setup

All experiments were conducted inside a temperature and pressure controlled stainless-steel environmental chamber (Kurt J. Lesker Company). The internal dimensions of the cubic chamber are 40.5 cm in length, width, and height. It was designed to maintain the saturated conditions for condensation experiments by eliminating non-condensable gases (NCGs) by preventing air leakage. Besides, a rope heater was wrapped around the chamber and heated its inner walls slightly above the vapor saturation temperature to prevent condensation on the inner walls. Low pressure transducer (MKS 925 MicroPirani) and high-pressure transducer (MKS Type 728A) are mounted at the top of the chamber to monitor the vapor pressure. The high-pressure gauge is accurate above 1 kPa, while the low-pressure gauge is accurate below 1kPa. The high-pressure gauge was calibrated by pumping the chamber down to nearly vacuum condition and adjusting the “ZERO” screw at the top of the high-pressure gauge until the readings reached 0 Pa.

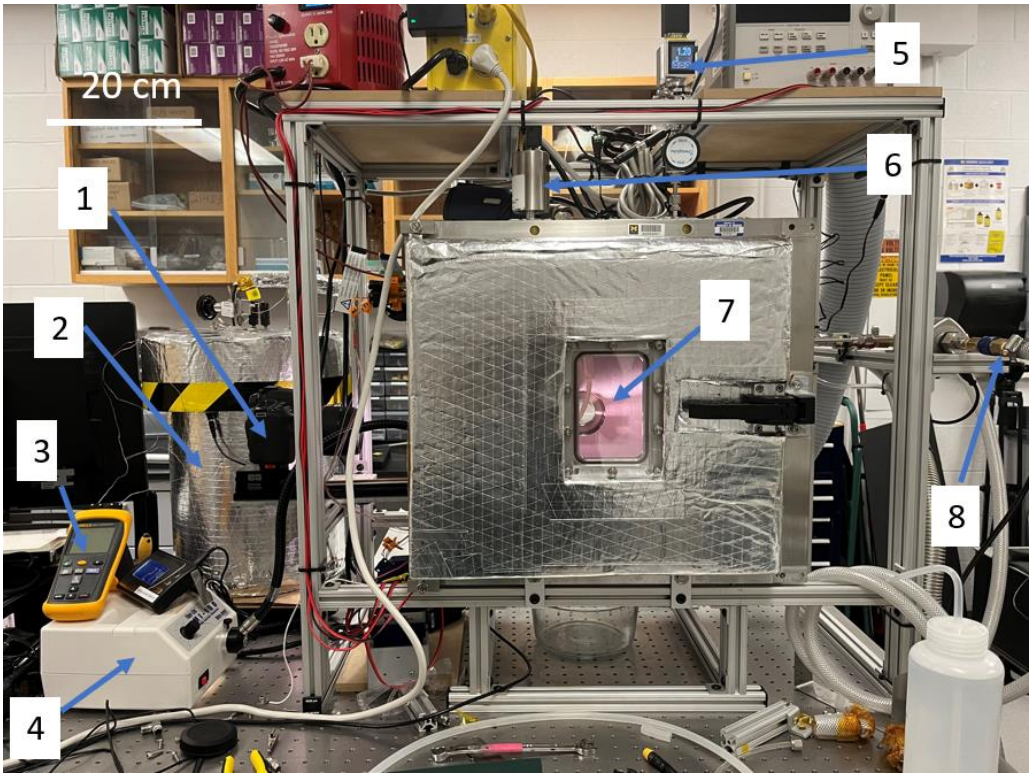

Figure 4. The front view of the environmental chamber and vapor generator. The cylinder in the left is the vapor generator and the cube in the right is the environmental chamber. Both the vapor generator and the environmental chamber are covered by fiberglass insulation. 1 is the camera, 2 is vapor generator, 3 is thermocouples measuring the vapor temperature inside the vapor generator, 4 is the light source, 5 is the low pressure transducer, 6 is the high pressure transducer, 7 is the environmental chamber and 8 is the cooling water tube from chiller.

A stainless-steel cylindrical vapor generator filled with water was built to supply hot saturated vapor to the environmental chamber. The vapor generator was covered and insulated externally using fiberglass insulation to minimize heat loss to the surrounding, enabling controlling of vapor temperature. Additionally, the vapor supply tube connecting vapor generator and environmental chamber is constantly heated by a rope heater to prevent condensation in the connecting flexible tube. A needle valve is mounted between the vapor supply tube and vapor generator to control the vapor flow rate entering the environmental chamber.

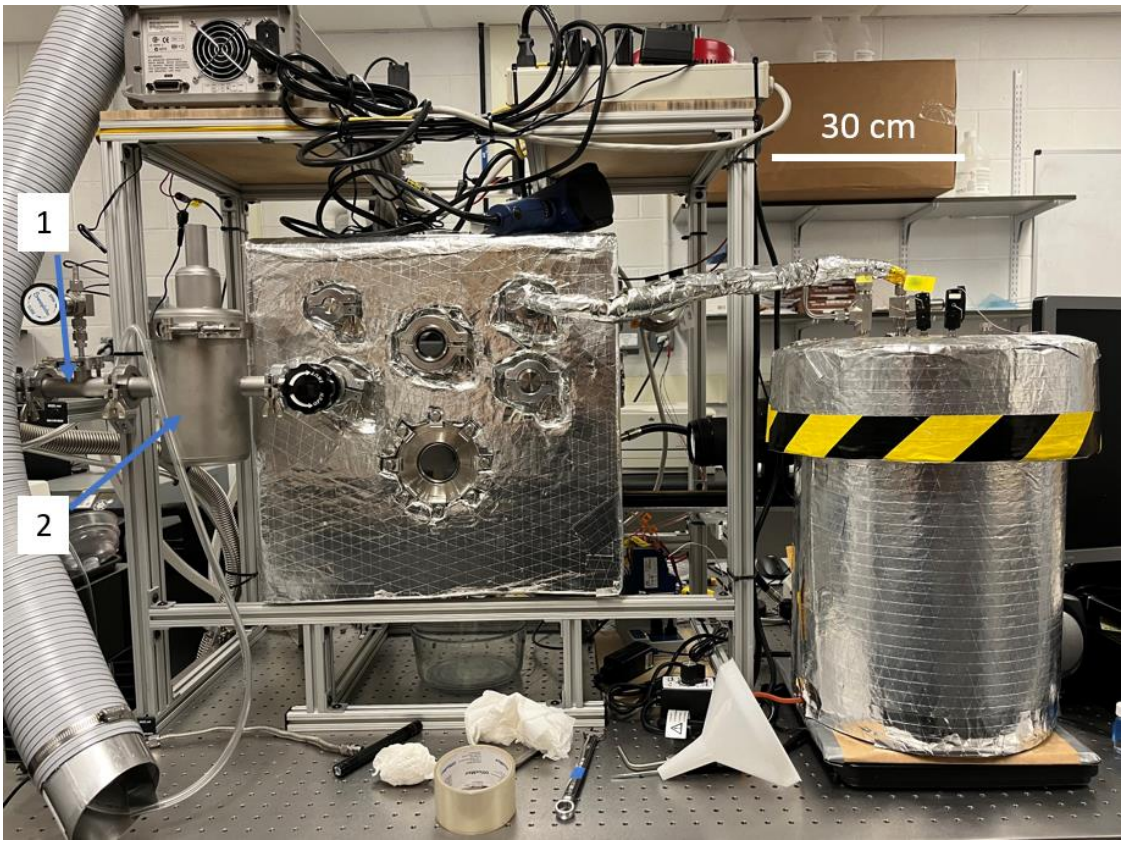

Figure 5. The back view of the environmental chamber and the vapor generator. They are connected through a flexible tube wrapped with rope heater to prevent condensation on the inner wall of the flexible tube. Before the experiment, the air (NCGs) will be evacuated by a vacuum pump, and the cold trap filled with liquid nitrogen is used to condense water vapor. 1 is the tube connected to vacuum pump and 2 is the cold trap

The insides view of the chamber is shown in Fig. 6. The sample tube is connected to the cooling system to bring away the heat generated during condensation and maintain a constant temperature difference with the vapor during the experiment. The inlet and outlet cooling water temperature and the cooling water flow rate are measured to calculate the heat transferred.

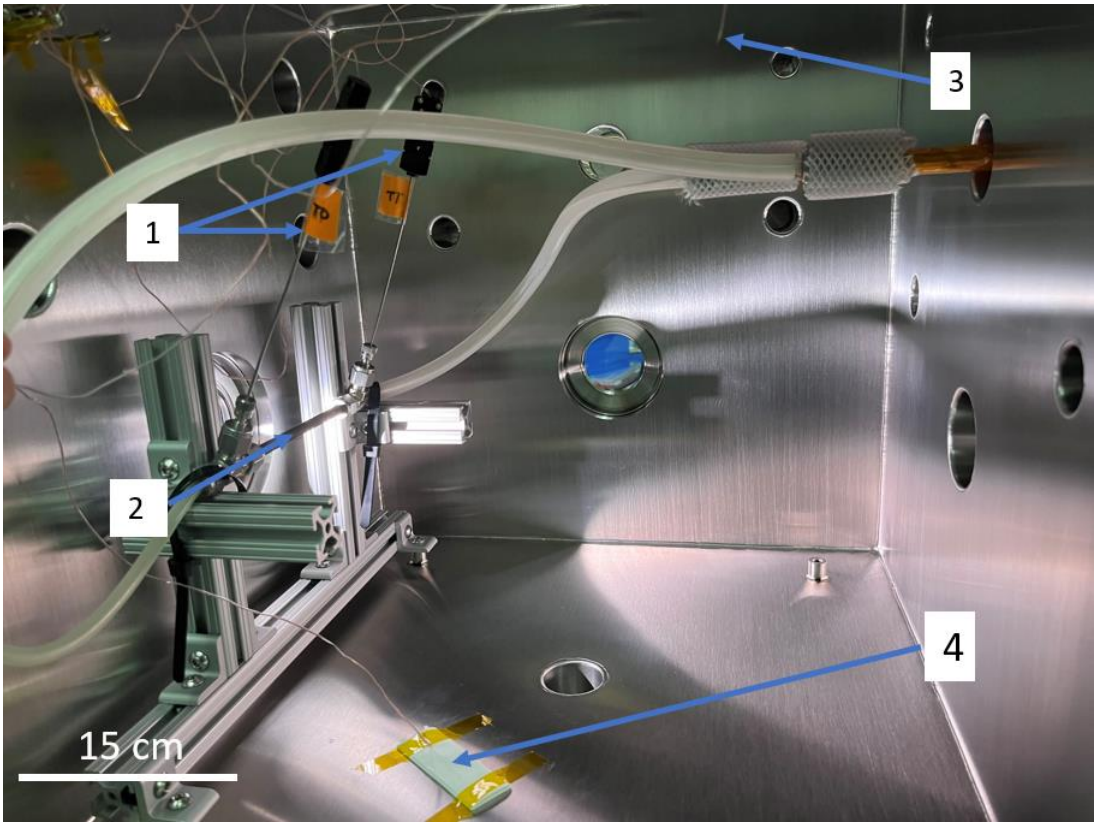

Figure 6. The inner view of the environmental chamber. Two calibrated thermocouples measure the inlet and outlet water temperature, from which we could get the heat flux of the condensation process. The wet-bulb thermocouple probe is imbedded in a wet cloth while the dry-bulb thermocouple probe is hanging from the top of the chamber and measure the vapor temperature away from the vapor inlet. 1 is the inlet and outlet cooling water thermocouples, 2 is the sample tube, 3 is the dry bulb thermocouple probe and 4 is the wet bulb thermocouple probe.

Thermocouples Calibration

The thermocouples were calibrated by relating the thermocouple readings with the actual temperature. During calibration, the thermocouples were immersed in the water tank of the chiller with ≤ 0.05 ºC accuracy. The temperature was maintained constant by recirculating the working fluid (water). After setting the chiller temperature and letting the water temperature stabilize (change ≤ 0.1 ºC/min), the data were collected using LabVIEW. By setting the temperature of chiller to different numbers ranging from 5 ºC to 25 ºC, data pairs consisting of thermocouple readings and actual temperature were obtained. Then, the actual temperature T_{act} and thermocouple readings $T_{reading}$ are related using curve fitting as:

$$T_{act} = \frac{T_{reading} - b}{a} \tag{4}$$

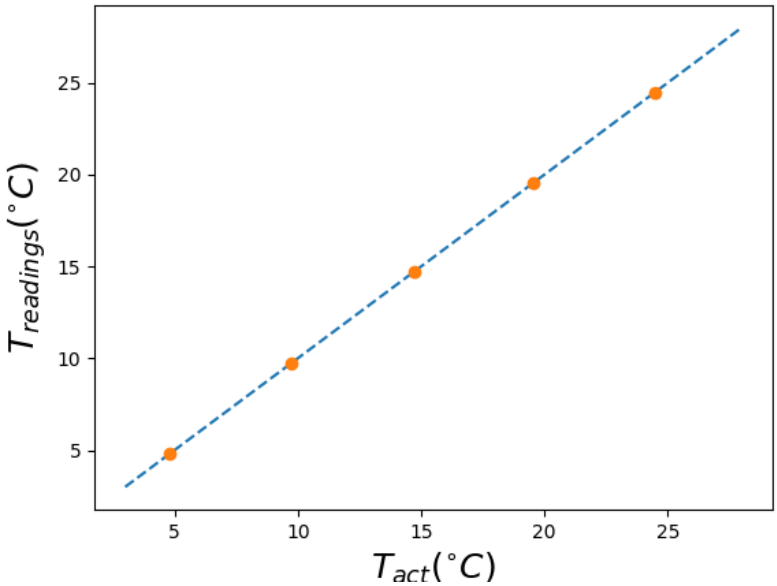

Figure 7. Thermocouples calibration curve. The actual temperature of the water bath versus the readings from the thermocouples. The two data are correlated linearly with 1% root-mean-square error (RMSE).

Experimental Procedure

Before the start of the experiment, the water inside the vapor generator needs to be degassed to remove NCGs. Firstly, the temperature inside the vapor generator was increased to ~130 ºC. Then, the valve is opened to allow the release of pressurized vapor into ambient air. This degassing procedure is repeated 4–5 times to make sure all NCGs are removed from the vapor generator. After degassing, the vapor generator was maintained at 130 ºC.

The sample tube was mounted on the stage and connected into the cooling circulating water from a chiller. At the beginning of the experiment, a vacuum pump is first started to evacuate the environmental chamber. The gas pumped out from the chamber pass through a cold trap filled with liquid nitrogen to capture water vapor, which would otherwise damage the vacuum pump. After the pressure inside the environmental chamber reaches ~150 Pa, the valve connecting the vacuum pump is closed and the vapor is introduced to the chamber from the vapor generator by opening the valve between vapor generator and the environmental chamber. When the chamber pressure reaches ~3 kPa, the valve connecting to the vacuum pump is reopened to remove the vapor. This process was repeated 3-4 times. The purpose of supplying and removing vapor is to quickly eliminate the NCGs inside the chamber by dissolving it with fresh vapor supplied from the vapor generator. This method is more efficient compared to waiting for the vacuum pump to create a nearly vacuum environment to eliminate the NCGs.

After eliminating NCGs, the vapor is fed into the chamber. When the condensation reaches the steady-state condition under a desired pressure, the data from thermocouples inside and the high-pressure gauge were collected using LabVIEW. The steady-state condition was reached when the

change in temperature from inlet, outlet, wet-bulb, and dry-bulb and chamber were ≤ 0.25 ºC/min and ≤ 0.1 kPa/min, respectively. The steady-state data are recorded for 3–5 min and time averaged to obtain a single data point in our experiments.

Measurement of the Heat Flux and Heat Transfer Coefficient

During the experiment, the temperature of the inlet cooling water, outlet cooling water, dry bulb wet bulb, and the chamber pressure were measured and recorded. We could calculate heat transfer per unit area (heat flux) and condensation-side heat transfer coefficient from these data[16].

The heat flux equals to the heat transferred to the cooling water per second divided by the tube's outer surface aera, which can be expressed using this equation:

$$q'' = \frac{\rho_w \dot{V} c_w (T_2 - T_1)}{\pi d_o L} \tag{5}$$

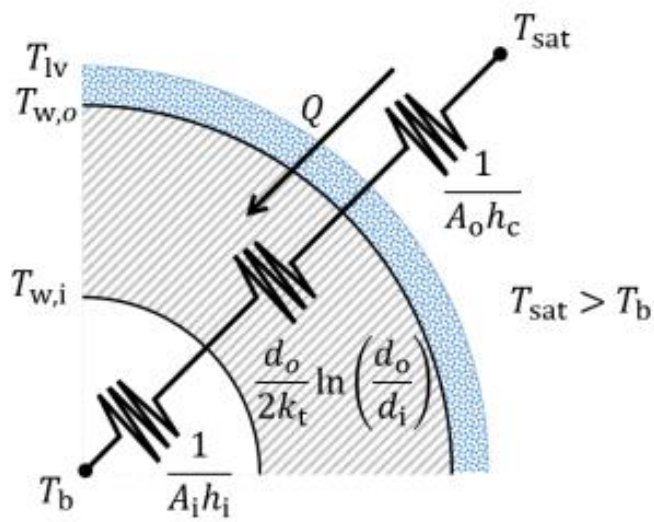

Figure 8. Three major thermal resistances for the tube condensation model[16]. The heat generated by the condensation process is finally brought away by the forced convection of the bulk cooling water.

More importantly, we want to know the heat transfer coefficient of the condensation process. The heat transfer coefficient can be calculated by considering the following two equations first:

$$\frac{T_{sat} - T_b}{Q} = \frac{T_{sat} - T_{w,o}}{Q} + \frac{T_{w,o} - T_{w,i}}{Q} + \frac{T_{w,i} - T_b}{Q} \tag{6}$$

$$Q = A \cdot U \cdot \Delta T \tag{7}$$

where T_b is the bulk temperature of the cooling water, $T_{w,i}$ is the inner tube wall temperature, $T_{w,o}$ is the outer tube wall temperature, T_{sat} is the vapor saturation temperature, Q is the heat transferred

per unit time, A is the surface aera and U is the heat transfer coefficient. The second term in the right-hand side of the Eq. 8 represents a conduction process across a cylindrical shell, which can be substitute by $(T_{w,o} - T_{w,i})/Q = \ln(d_o/d_i)/(2\pi L k_t)$, where $d_o, d_i, L,$ and k_t are the outer diameter, inner diameter, length and thermal conductivity of the tube, respectively. By substituting $\Delta T/Q$ with $1/(UA)$ (thermal resistance) for the remaining terms, we could get the following equation:

$$\frac{1}{A_o U_o} = \frac{1}{A_o h_c} + \frac{\ln(d_o/d_i)}{2\pi L k_t} + \frac{1}{A_i h_i} \tag{8}$$

where $A_o$and A_i are the outer and inner surface area of the sample tube, U_o, h_i, and h_c are the overall, internal and condensation heat transfer, respectively. Rearranging Eq. 8, we could calculate the condensation heat transfer coefficient using this equation:

$$h_c = \left(\frac{1}{U_o} - \frac{A_o}{A_i h_i} - \frac{A_o \ln(d_o/d_i)}{2\pi L k_t}\right)^{-1} \tag{9}$$

We could estimate the overall heat transfer coefficient U_o from the heat flux and the logarithmic mean temperature difference ΔT_{LMTD}:

$$U_o = \frac{q''}{\Delta T_{LMTD}} \tag{10}$$

$$\Delta T_{LMTD} = \frac{(T_2 - T_{sat}) - (T_1 - T_{sat})}{\ln\left(\frac{T_2 - T_{sat}}{T_1 - T_{sat}}\right)} \tag{11}$$

where T_{sat} is the saturation temperature difference, which can be calculated by averaging the dry bulb and wet bulb temperatures.

The internal heat transfer coefficient is calculated by fist considering the Reynolds number Re_D:

$$Re_D = \frac{4\dot{V}\rho_w}{\pi d_i u_w} \tag{12}$$

where u_w is the viscosity of the cooling water and ρ_w is the water density. In this experiment, we usually use 2.6 L/min flow rate, which results in a turbulent flow with Re_D > 10000. This friction factor f of the turbulent flow can be calculated using Petukhov's correlation[20]:

$$f = (0.790\, ln(Re_D) - 1.64)^{-2} \tag{13}$$

Using Gnielinski correlation[21], we could then further calculate the Nusselt number Nu_D from the friction factor, Prandtl number ($Pr = c_p \mu_w / k_w$) and Reynolds number:

$$Nu_D = \frac{(f/8)(Re_D - 1000)Pr}{1 + 12.7(f/8)^{\frac{1}{2}}\left(Pr^{\frac{2}{3}} - 1\right)}, 0.5 < Pr < 10^6,\ 3000 < Re_D < 10^6 \tag{14}$$

Finally, the internal heat transfer coefficient is calculated as:

$$h_i = \frac{Nu_D k_w}{d_i} \tag{15}$$

Results and Discussion

Following the experimental procedure and using the equations listed above, we maintained the vapor pressure inside the environmental chamber at 2.5–4.2 kPa and the cooling water temperature between 16–23 ℃ to get different subcooling temperature and collect data under different subcooling temperatures. The subcooling temperature equal to the saturation temperature of vapor minus the calculated outer wall temperature.

Filmwise condensation

A smooth and untreated copper tube is wet cleaned using acetone, ethanol, IPA, and deionized water and plasma treated for 15 minutes for FWC experiments. The photo for FWC is shown in Fig 9.

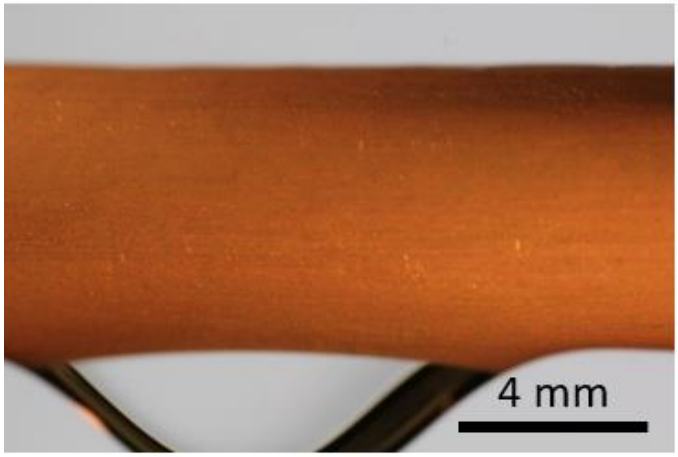

Figure 9. Filmwise condensation on the hydrophilic tube.

The heat flux as a function of subcooling temperature for FWC is shown in Fig. 10 (a). The slope of the heat flux curve is the heat transfer coefficient, which is shown in Fig. 10 (b). The red curve in both figures represent the Nusselt model[17] prediction. As for FWC, both the heat flux and heat transfer coefficient agree well with the Nusselt model.

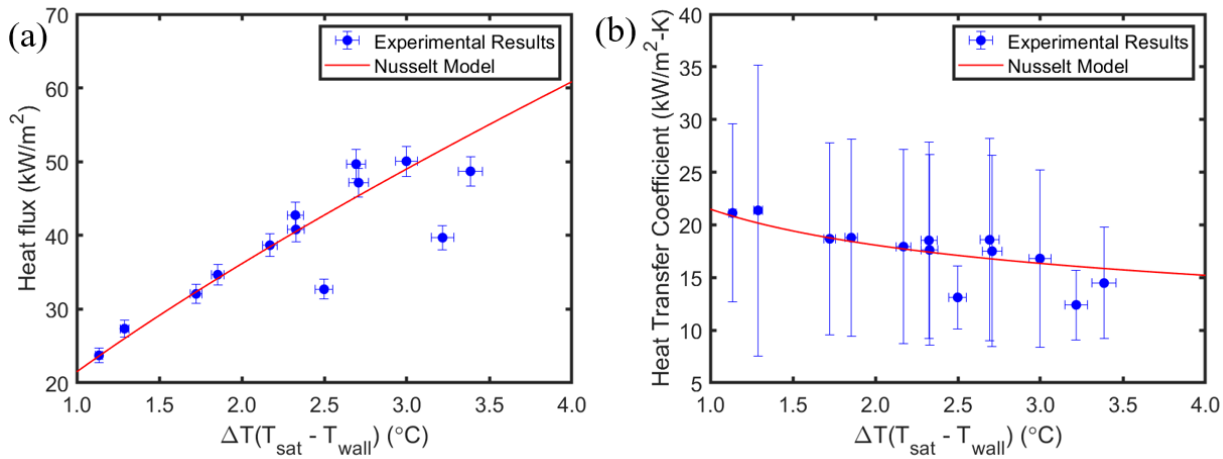

Figure 10. The heat flux and heat transfer coefficient as a function of subcooling (chamber vapor saturation temperature minus outer tube wall temperature) for FWC. The red curve represents the Nusselt model.

Dropwise condensation

Superhydrophobic surfaces

After immersing in silver nitrate aqueous solution and heptadecafluoro-1-decanethiol dichloromethane solution, the smooth and hydrophilic copper tube becomes superhydrophobic with water contact angle of 167 º. The condensation mode on it became dropwise condensation. Fig. 11 (a) shows the heat flux as a function of subcooling temperature, and the corresponding heat transfer coefficient is shown in Fig 10 (b).

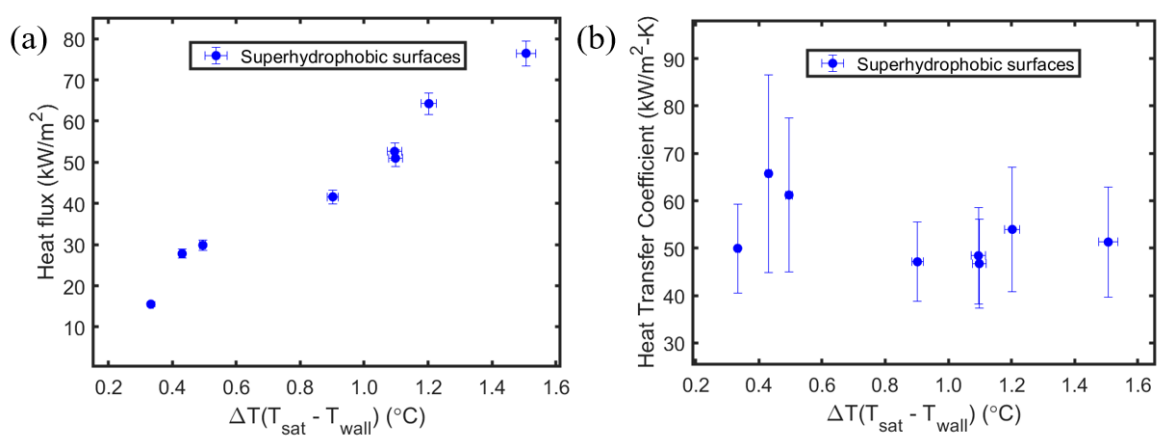

Figure 11. The heat flux and heat transfer coefficient as a function of subcooling for dropwise condensation on a superhydrophobic tube with water contact angle of 167 º. The averaged heat transfer coefficient is 53 $\mathrm{kW/m^2K}$.

The averaged heat transfer coefficient for dropwise condensation on superhydrophobic copper tube is 53 $\mathrm{kW/m^2 \cdot K}$, nearly 3 times higher than the filmwise condensation (17 $\mathrm{kW/m^2 \cdot K}$). This enhancement in heat transfer coefficient is mainly because that the condensed water form discrete droplets, which allows the direct contact between water vapor and cold copper surface.

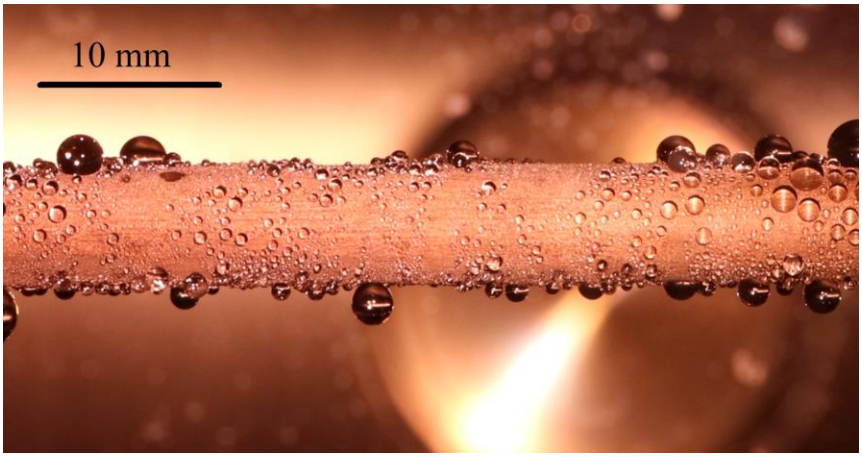

Figure 12. Dropwise condensation on the superhydrophobic tube.

SLIPS Condensation

After coating a thin lubricant oil film on the previously made superhydrophobic tube, we obtained the SLIPS tube. The measured heat transfer coefficient for SLIPS is only $6\ \mathrm{kW/m^2 \cdot K}$, even significantly lower than the $17\ \mathrm{kW/m^2 \cdot K}$ for filmwise condensation. The measured advancing and receding contact angles of smooth copper surface, superhydrophobic surface and SLIPS are shown in Table 1. The superhydrophobic surface and SLIPS are fabricated using the same method as the sample tubes.

Table 1. Advancing and receding contact angle for water on the hydrophilic [7], hydrophobic, and SLIP surfaces.

Surface type	**Advancing angle**	**Receding angle**
Hydrophilic (smooth copper)	≈ 0 º	≈ 0 º
Superhydrophobic	174 ± 3 º	158 ± 3 º
SLIPS	118 ± 2 º	114 ± 3 º

The SLIPS has an extremely low contact angle hysteresis and thus a higher droplet mobility compared to the superhydrophobic surfaces used in this work. Therefore, according to the theory, the heat transfer coefficient on SLIPS should be higher than the typical dropwise condensation due to the smaller departure radius and higher departure frequency brought by the extremely high droplet mobility[18]. One possible reason is the pinning of droplet on SLIPS. Due to fabrication defects or the depletion of oil, the water droplet severely pins on the tube, which significantly increases the droplet departure radius and decreases the departure frequency, as shown in Fig. 13.

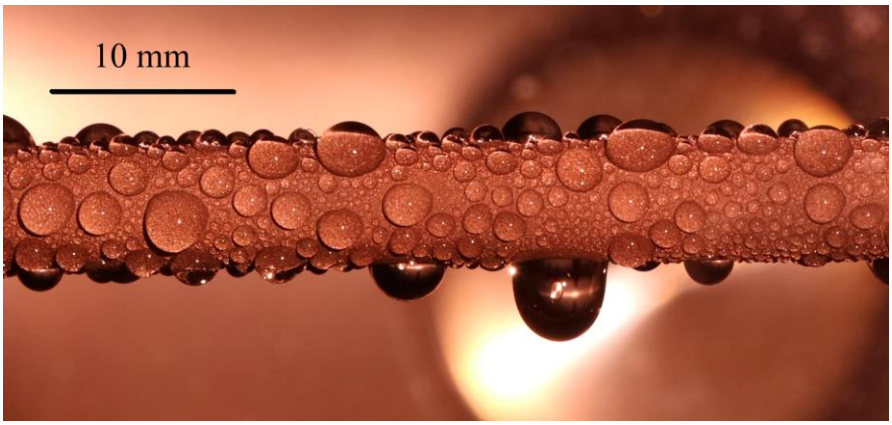

Figure 13. SLIPS Condensation. The droplets are pinned on the surface and have a relatively large departure radius.

Summary and Future Work

After the training on condensation experiments during this summer, I become familiar with not only the heat transfer model and theory for the condensation on a tube, but also the detailed experimental procedure of measuring heat flux and heat transfer coefficient during phase change condensation in a temperature and pressure controlled environmental chamber. In this work, we measure the heat flux and heat transfer coefficient of a smooth and untreated hydrophilic copper tube, a superhydrophobic copper tube and a SLIPS copper tube using a custom-made environmental chamber and vapor generator. The measured heat transfer coefficient for filmwise condensation is 17 $\mathrm{kW/m^2 \cdot K}$. In our experiments, the heat transfer coefficient for dropwise condensation was 53 $\mathrm{kW/m^2 \cdot K}$, a nearly three-fold increase in phase change heat transfer rate. However, for SLIPS, the measured heat transfer coefficient lower than anticipated based on the current understanding of oil-impregnated surfaces (SLIPS). The possible explanation for the lower than anticipated heat transfer rate is attributed to the pinning of droplets on the condensing surface. The fabrication defects and the depletion of oil are also expected to contribute to contact line pinning during droplet nucleation, growth, and departure. Past studies have shown that the SLIPS has a significantly smaller contact angle hysteresis compared to the superhydrophobic surfaces, which implies higher heat transfer rate unlike the results obtained in this study. In the future, we plan to make a new SLIPS tube and measure its heat transfer coefficient until we get consistent and reasonable results. After that, we will study the effect of lubricant oil viscosity on the heat transfer coefficient for SLIPS. Since a higher oil viscosity will result in a smaller wetting ridge for the departure droplet, it will be helpful in decreasing the oil depletion rate and improving the working time of the SLIPS tube. To date, the effect of lubricant viscosity of heat transfer rate is not reported.

Reference

1 Kim, H. & Nam, Y. Condensation behaviors and resulting heat transfer performance of nano-engineered copper surfaces. *International journal of heat and mass transfer* **93**, 286-292 (2016).

2 Miljkovic, N., Enright, R. & Wang, E. N. Effect of droplet morphology on growth dynamics and heat transfer during condensation on superhydrophobic nanostructured surfaces. *ACS nano* **6**, 1776-1785 (2012).

3 Kaushik, S., Reddy, V. S. & Tyagi, S. Energy and exergy analyses of thermal power plants: A review. *Renewable and Sustainable energy reviews* **15**, 1857-1872 (2011).

4 Carey, V. P. *Liquid-vapor phase-change phenomena: an introduction to the thermophysics of vaporization and condensation processes in heat transfer equipment*. (CRC Press, 2020).

5 Wen, R., Ma, X., Lee, Y.-C. & Yang, R. Liquid-vapor phase-change heat transfer on functionalized nanowired surfaces and beyond. *Joule* **2**, 2307-2347 (2018).

6 Cho, H. J., Preston, D. J., Zhu, Y. & Wang, E. N. Nanoengineered materials for liquid–vapour phase-change heat transfer. *Nat Rev Mater* **2**, 1-17 (2016).

7 Nusselt, W. Die oberflachenkondensation des wasserdamphes. *VDI-Zs* **60**, 541 (1916).

8 Rothstein, J. P. Slip on superhydrophobic surfaces. *Annual review of fluid mechanics* **42**, 89-109 (2010).

9 Schmidt, E., Schurig, W. & Sellschopp, W. Versuche über die Kondensation von Wasserdampf in Film-und Tropfenform. *Technische Mechanik und Thermodynamik* **1**, 53-63 (1930).

10 Rose, J. Dropwise condensation theory and experiment: a review. *Proceedings of the Institution of Mechanical Engineers, Part A: Journal of Power and Energy* **216**, 115-128 (2002).

11 Khandekar, S. & Muralidhar, K. *Dropwise condensation on inclined textured surfaces*. (Springer, 2014).

12 Aili, A., Ge, Q. & Zhang, T. How nanostructures affect water droplet nucleation on superhydrophobic surfaces. *Journal of Heat Transfer* **139** (2017).

13 Li, G. *et al.* Microscopic droplet formation and energy transport analysis of condensation on scalable superhydrophobic nanostructured copper oxide surfaces. *Langmuir* **30**, 14498-14511 (2014).

14 Zheng, S., Eimann, F., Philipp, C., Fieback, T. & Gross, U. Modeling of heat and mass transfer for dropwise condensation of moist air and the experimental validation. *International Journal of Heat and Mass Transfer* **120**, 879-894 (2018).

15 Kim, S. & Kim, K. J. Dropwise condensation modeling suitable for superhydrophobic surfaces. (2011).

16 Bhuyan, D. Direct and Indirect Contact Filmwise as well as Dropwise Condensation of Water Vapour with and without Noncondensible Gas-A Review. (2020).

17 Wong, T.-S. *et al.* Bioinspired self-repairing slippery surfaces with pressure-stable omniphobicity. *Nature* **477**, 443-447 (2011).

18 Preston, D. J. *et al.* Heat transfer enhancement during water and hydrocarbon condensation on lubricant infused surfaces. *Scientific reports* **8**, 1-9 (2018).

19 Adera, S. *et al.* Enhanced condensation heat transfer using porous silica inverse opal coatings on copper tubes. *Scientific reports* **11**, 1-11 (2021).

20 Kothandaraman, C. *Fundamentals of heat and mass transfer*. (New Age International, 2006).

21 Gnielinski, V. New equations for heat and mass transfer in turbulent pipe and channel flow. *Int. Chem. Eng.* **16**, 359-368 (1976).